ACS APPLIED MATERIALS & INTERFACES

www.acsami.org Research Article

# Strain-Induced Ultrahigh Electron Mobility and Thermoelectric Figure of Merit in Monolayer $\alpha$-Te

Jinlong Ma, Fanchen Meng, Jian He, Yu Jia, and Wu Li*

Cite This: *ACS Appl. Mater. Interfaces* 2020, 12, 43901−43910 Read Online

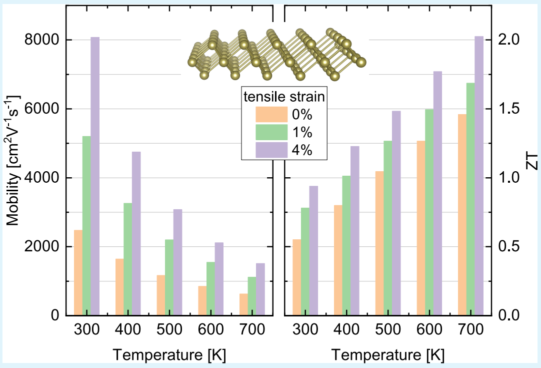

**ABSTRACT:** In line with the classic phonon-glass electron-crystal (PGEC) paradigm, semiconducting and semimetallic multinary compounds remain the cornerstone of the state-of-the-art thermoelectric materials. By contrast, elemental PGEC is very rare. In this work, we report a thermoelectric study of monolayer $\alpha$-Te by first-principles calculations and solving the parameter-free Boltzmann transport equation. It is found that monolayer $\alpha$-Te possesses high electron mobility (about 2500 cm$^2$ V$^{-1}$ s$^{-1}$) at room temperature due to small effective mass, low phonon frequencies, and thus a restricted phase space for electron−phonon scattering. In monolayer $\alpha$-Te, the electrons near the conduction band edge are mainly scattered by the heavily populated quadratically dispersing out-of-plane acoustic (ZA) phonon modes. The thermoelectric figure of merit ($ZT$) for $n$-type monolayer $\alpha$-Te is 0.55 at 300 K and 1.46 at 700 K. Notably, tensile strain stiffens the ZA modes, yielding a linear energy-momentum dispersion relation and the removal of the diverging thermal population of ZA phonons. Consequently, the electron mobility is enhanced. At a 4% tensile strain, the electron mobility can reach up to 8000 cm$^2$ V$^{-1}$ s$^{-1}$ at room temperature while the thermal conductivity is almost unaffected, yielding a state-of-the-art $ZT$ value of 0.94 and 2.03 in n-type monolayer $\alpha$-Te at 300 and 700 K, respectively. For completeness, the thermoelectric study of p-type monolayer $\alpha$-Te is also conducted. These results beckon further experiments toward high-performance $\alpha$-Te-based thermoelectric materials via doping, alloying, and compositing.

**KEYWORDS:** *high mobility, thermoelectric, 2D material, strain effect, Te*

## 1. INTRODUCTION

Broader application of thermoelectrics calls for high-performance thermoelectric (TE) materials; the performance of a TE material is gauged by its dimensionless figure of merit, $ZT = \frac{\sigma S^2 T}{\kappa_e + \kappa_L}$,[1,2] where $\sigma$, $S$, $\kappa_e$, and $\kappa_L$ are the electrical conductivity, Seebeck coefficient, electronic thermal conductivity, and lattice thermal conductivity, respectively. Toward high $ZT$ values, the materials must simultaneously possess low total thermal conductivity $\kappa$ ($\kappa = \kappa_e + \kappa_L$) along with high electrical conductivity and a high Seebeck coefficient in line with the phonon-glass electron-crystal (PGEC) paradigm. Though there is no known upper limit for $ZT$, most state-of-the-art TE materials have their peak $ZT$ values between 2 and 3 due to the adverse interdependence among $\{\sigma, S, \kappa_e\}$; optimizing one property generally degrades others.[2] Hence, TE material research is a delicate game of trade-offs and synergy.[3] To ease the adversely interdependent $\{\sigma, S, \kappa_e\}$, besides the classic PGEC approach, one notable approach is pursuing high $ZT$ values in the material systems with reduced dimensionality by means of classical and quantum size effects. The classical size effects are related to the limitation of the phonon mean-free path via scattering, while the quantum size effects arise from the change in the electronic band structure, e.g., singularities in the density of states, and phonon dispersion relation due to quantum confinement.[4,5] The size effects can make a material with reduced dimensionality so distinct from its bulk counterpart that the material with reduced dimensionality is treated as a new material despite the same composition and the crystal structure.

Specifically, two-dimensional (2D) materials have attracted tremendous interests from the point of view of reduced dimensionality as they can be cleaved or made nanosized. In the field of TE material research, 2D materials such as transition metal dichalcogenides (TMDs)[6,7] have demonstrated their promise by possessing a large power factor (PF = $\sigma S^2$) comparable with the state-of-the-art bulk TE materials. On the other hand, TMDs often have thermal conductivities, too high for good thermoelectrics. In parallel with the experimental study, theoretical calculations, typically involved with simplifications on an electronic band structure and a scattering

**Received:** June 9, 2020
**Accepted:** September 1, 2020
**Published:** September 1, 2020

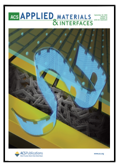

https://dx.doi.org/10.1021/acsami.0c10236
*ACS Appl. Mater. Interfaces* 2020, 12, 43901−43910

rate, have been carried out to explore the TE promise of many 2D materials including $MX_2$ (M = Mo, W; X = S, Se),[8−10] $MCO_2$ (M = Ti, Zr, Hf),[11] $TiS_2$,[12] $ZrS_2$,[13] $TiS_3$,[14] black phosphorene,[15] PdXY (X, Y = S, Se, Te),[16,17] and $Bi_2Te_2X$ (X = S, Se, Te),[18] to name a few. The results of these calculations do not yield *ZT* values above unity due to a low power factor and/or high thermal conductivity. Recently, promisingly high *ZT* values are predicted in emerging 2D materials, such as $PbI_2$,[19] KAgSe,[20] and pentasilicene.[21] Nonetheless, the phenomenological models with simplifications generally lack enough predictive power. Hence, there is a demanding need for first-principles (parameter-free) calculations of the performance of TE materials.

From the computation perspective, the materials to be modeled would be structurally simple enough so the results are reliable yet thermoelectrically good enough so the results are of immediate practical implication. Elemental Te is such a material. Recently, Lin et al.[22] reported polycrystalline bulk Te as a good TE material with *ZT* up to 1.0 at 600 K. *ZT* = 1.0 is regarded as the benchmark for practical TE materials. This discovery is ground breaking in that most known good TE materials are multinary semiconductors or semimetals, whereas Te is elemental. On the other hand, the experimental results of Te are derived from polycrystalline samples, which does not fully reflect the thermoelectric potential of Te, given its anisotropic crystal structure. Hence, inspired by the reduced dimensionality approach mentioned above and in the light of the layered crystal structure of Te, the intrinsic TE performance of monolayer Te needs to be studied.

To this end, Zhu et al.[23] predicted that monolayer Te could possess two semiconductor phases, named $\alpha$-Te and $\beta$-Te using density functional theory (DFT) calculations. The $\alpha$-Te phase is stable, whereas $\beta$-Te is metastable.[23] The authors also pointed out that monolayer $\alpha$-Te could be readily obtained via a thickness-dependent structural phase transition along the [001] direction of the trigonal bulk Te, whereas the $\beta$-Te phase could be derived by the structural relaxation when the bulk helical chain structure is truncated along the equivalent [010] or [100] direction. So far, only the $\beta$-Te phase has been experimentally obtained using molecular beam epitaxy growth on a highly oriented pyrolytic graphite (HOPG) substrate[23,24] and a graphene/6H-SiC substrate.[25] The interactions from the substrate during Te growth prevent $\beta$-Te from transforming into a more stable $\alpha$ phase. Nonetheless, when grown on a substrate that is more chemically bounded (yet not too strong) than HOPG and graphene/6H-SiC substrate, $\alpha$-Te is expected.[23]

Regarding the thermoelectric performance of monolayer Te, previous studies showed that $\kappa_L$ of $\alpha$- and $\beta$-Te are lower than 10 W $m^{-1}$ $K^{-1}$ above room temperature,[26−28] much smaller than that of monolayer TMDs.[29,30] Nonetheless, the studies of full thermoelectric transport properties are scarce. The electrical transport properties in previous studies are estimated based on a roughly constant relaxation time,[27,28] which in real life depends on carrier modes, carrier concentrations, and temperatures. Therefore, more accurate study is highly desired. To accurately calculate the electrical transport properties, first-principles calculations have not been made possible until recently by solving the Boltzmann transport equations (BTE) with scattering limited by the electron−phonon interactions obtained from DFT and density functional perturbation theory (DFPT).[31−35] Electron−phonon interactions are typically the dominant mechanism at an elevated temperature, where the *ZT* value peaks. In this work, we calculate full thermoelectric transport properties along with *ZT* of the monolayer $\alpha$-Te from first principles and parameter-free BTE. Considering the fact that the monolayer Te is grown on a substrate, mismatch in the lattice constants could result in strain, either compressive or tensile; the strain effect is studied.

## 2. METHODOLOGY

In an external electric field **E**, the electron distribution is deviated from the equilibrium, whereas the scattering tends to restore the equilibrium. The steady state is described by the BTE as

$$-\frac{e\mathbf{E}}{\hbar}\frac{\partial f_{n\mathbf{k}}}{\partial \mathbf{k}} + \mathcal{I}_{\text{scatt}}(f_{n\mathbf{k}}) = 0 \tag{1}$$

where $\hbar$ is the reduced Plank constant, $e$ is the elemental charge, and $f_{n\mathbf{k}}$ is the distribution of an electron state at a wave vector **k** with a band index $n$. For weak **E**, the electron distribution deviates only slightly from the equilibrium; thus, we can expand $f_{n\mathbf{k}}$ around the equilibrium Fermi−Dirac distribution, $f^0_{n\mathbf{k}}$, and keep only the linear terms in **E**, as[34]

$$f_{n\mathbf{k}} = f^0_{n\mathbf{k}} + e\mathbf{E}\cdot\mathbf{F}_{n\mathbf{k}}\left(-\frac{\partial f^0_{n\mathbf{k}}}{\partial \epsilon_{n\mathbf{k}}}\right) \tag{2}$$

where $\epsilon_{n\mathbf{k}}$ is the electron energy. Then, when the scattering is limited by electron−phonon coupling, the BTE can be linearized as[34]

$$\mathbf{F}_{n\mathbf{k}} = \mathbf{v}_{n\mathbf{k}}\tau_{n\mathbf{k}} + \tau_{n\mathbf{k}}\sum_{\mathbf{q}qpqm} W^{m\mathbf{k}+\mathbf{q}}_{n\mathbf{k},\mathbf{q}p}\mathbf{F}_{n\mathbf{k}+\mathbf{q}} \tag{3}$$

where $W^{m\mathbf{k}+\mathbf{q}}_{n\mathbf{k},\mathbf{q}p}$ is the transition probability by absorbing or emitting a phonon with a wave vector **q** and a mode index $p$, as[34]

$$\begin{aligned} W^{m\mathbf{k}+\mathbf{q}}_{n\mathbf{k},\mathbf{q}p} = \frac{2\pi}{\hbar}|g^{m\mathbf{k}+\mathbf{q}}_{n\mathbf{k},\mathbf{q}p}|^2 \times [(n^0_{\mathbf{q}p} + f^0_{m\mathbf{k}+\mathbf{q}}) \\ \delta(\epsilon_{n\mathbf{k}} + \hbar\omega_{\mathbf{q}p} - \epsilon_{m\mathbf{k}+\mathbf{q}}) + (1 + n^0_{\mathbf{q}p} - f^0_{m\mathbf{k}+\mathbf{q}}) \\ \delta(\epsilon_{n\mathbf{k}} - \hbar\omega_{\mathbf{q}p} - \epsilon_{m\mathbf{k}+\mathbf{q}})] \end{aligned} \tag{4}$$

and $\tau_{n\mathbf{k}}$ is the relaxation time calculated from

$$\frac{1}{\tau_{n\mathbf{k}}} = \sum_{\mathbf{q}qpqm} W^{m\mathbf{k}+\mathbf{q}}_{n\mathbf{k},\mathbf{q}p} \tag{5}$$

where $n^0_{\mathbf{q}p}$ is the Bose−Einstein distribution for a phonon, $\omega_{\mathbf{q}p}$ is the phonon frequency, $g^{\mathbf{q}p}_{n\mathbf{k},m\mathbf{k}+\mathbf{q}}$ is the electron−phonon coupling strength,[31,36]

$$g^{m\mathbf{k}+\mathbf{q}}_{n\mathbf{k},\mathbf{q}p} = \frac{1}{\sqrt{2\omega_{\mathbf{q}p}}}\langle\psi_{m\mathbf{k}+\mathbf{q}}|\partial V_{\mathbf{q}p}|\psi_{n\mathbf{k}}\rangle \tag{6}$$

where $\partial V_{\mathbf{q}p}$ is the perturbation of self-consistent potential due to lattice vibration, and $\psi_{n\mathbf{k}}$ is the electronic wavefunction.

$\mathbf{F}_{n\mathbf{k}}$ can be obtained by iteratively solving eq 3,[34] then $f_{n\mathbf{k}}$ is known. From the current density expression

$$\mathbf{J} = \boldsymbol{\sigma}\mathbf{E} = \frac{se}{VN_k}\sum_{n\mathbf{k}} f_{n\mathbf{k}}\mathbf{v}_{n\mathbf{k}} \tag{7}$$

the electrical conductivity is calculated as[32,34,37]

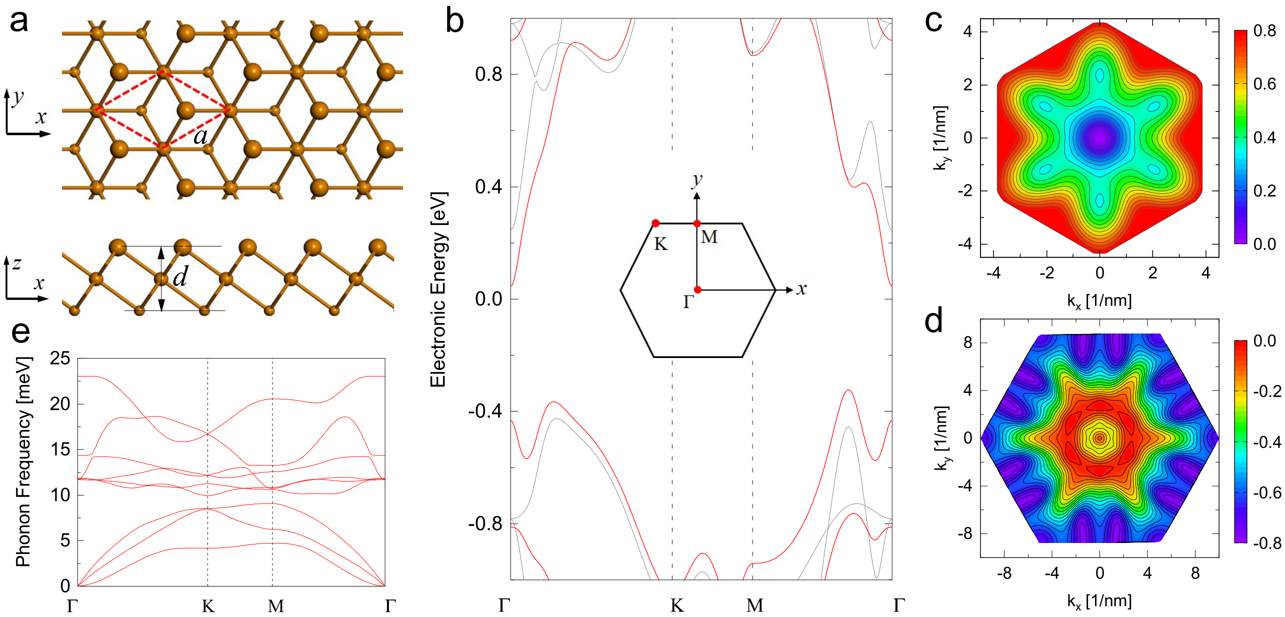

**Figure 1.** (a) Top and side views of the crystal structure of monolayer $\alpha$-Te with the primitive cell indicated by the red dashed lines. (b) Electronic band structure with (red) and without (gray) the spin-orbital coupling effect along high symmetry directions of reciprocal space shown in the inset. The electronic energy versus the wave vector for the (c) conduction band and the (d) valence band around the band edge. (e) Phonon dispersion including spin-orbital coupling along high symmetry directions.

$$\boldsymbol{\sigma} = \frac{se^2}{VN_\mathrm{k}} \sum_{n\mathbf{k}} \mathbf{v}_{n\mathbf{k}} \mathbf{F}_{n\mathbf{k}} \left( -\frac{\partial f^0_{n\mathbf{k}}}{\partial \epsilon_{n\mathbf{k}}} \right) \tag{8}$$

where $s$ is the number of carriers per state, $V$ is the volume of the unit cell, $N_\mathrm{k}$ is the **k** meshes of the first Brillouin zone. The mobility can be obtained by dividing the electrical conductivity by the carrier concentration $n_\mathrm{c}$, as

$$\boldsymbol{\mu} = \frac{\boldsymbol{\sigma}}{en_\mathrm{c}} \tag{9}$$

with $n_\mathrm{c} = \frac{s}{VN_\mathrm{k}} \sum_{n\mathbf{k}} f^0_{n\mathbf{k}}$ for the n-type system and $n_\mathrm{c} = \frac{s}{VN_\mathrm{k}} \sum_{n\mathbf{k}} (1 - f^0_{n\mathbf{k}})$ for the p-type system. The Seebeck coefficient can also be calculated from[37]

$$\boldsymbol{\sigma}\mathbf{S} = \frac{se}{TVN_\mathrm{k}} \sum_{n\mathbf{k}} (\epsilon_{n\mathbf{k}} - \epsilon_\mathrm{f}) \mathbf{v}_{n\mathbf{k}} \mathbf{F}_{n\mathbf{k}} \left( -\frac{\partial f^0_{n\mathbf{k}}}{\partial \epsilon_{n\mathbf{k}}} \right) \tag{10}$$

and the electronic thermal conductivity is obtained by[37]

$$\boldsymbol{\kappa}_\mathrm{e} = \frac{s}{TVN_\mathrm{k}} \sum_{n\mathbf{k}} (\epsilon_{n\mathbf{k}} - \epsilon_\mathrm{f})^2 \mathbf{v}_{n\mathbf{k}} \mathbf{F}_{n\mathbf{k}} \left( -\frac{\partial f^0_{n\mathbf{k}}}{\partial \epsilon_{n\mathbf{k}}} \right) - T\boldsymbol{\sigma}\mathbf{S}^2 \tag{11}$$

where $T$ is the temperature and $\epsilon_\mathrm{f}$ is the chemical potential.

The lattice thermal conductivity is calculated in an analogous framework of BTE for phonons, as[38,39]

$$\boldsymbol{\kappa}_\mathrm{L} = \frac{1}{VN_\mathrm{q}} \sum_{\mathbf{q}p} \hbar\omega_{\mathbf{q}p} \mathbf{v}_{\mathbf{q}p} \mathbf{F}_{\mathbf{q}p} \frac{\partial n^0_{\mathbf{q}p}}{\partial T} \tag{12}$$

where $N_\mathrm{q}$ is the number **q** grids, $\mathbf{v}_{\mathbf{q}p}$ is the phonon group velocity, and $\mathbf{F}_{\mathbf{q}p}$ is phonon mean-free displacement, which is obtained from an iterative solution of BTE.[38]

In this work, the DFT and DFPT calculations were carried out in the Quantum ESPRESSO package[40] using full-relativistic norm-conserving pseudopotentials with local density approximation (LDA) exchange−correlation functional.[41] Figure 1a shows the crystal structure of monolayer $\alpha$-Te in the Cartesian space, which adopts a trigonal $P\bar{3}m1$ (#164) space group. The relaxed lattice constant is $a$ = 4.14 Å, in agreement with the literature data.[23,27] In a side view, there are three Te atomic planes, with a distance between the upper and lower atomic planes of $d$ = 3.60 Å. The crystal structure is not mirror symmetrized with respect to the middle atomic plane. The vacuum space perpendicular to the atomic plane was fixed to be 20 Å to eliminate the interactions between layers. For the properties normalized by volume, an effective thickness of 7.72 Å was adopted, as known as the distance between surface Te atomic planes plus the van der Waals radii of a Te atom.[27] The electron energy, phonon dispersion, and electron−phonon coupling were initially calculated on 8 × 8 × 1 **k** and 8 × 8 × 1 **q** grids. To calculate electrical transport properties, Wannier function interpolation was employed as implemented in EPW package.[36] To calculate $\kappa_\mathrm{L}$, the third-order anharmonic interatomic force constants were calculated using a 4 × 4 × 1 supercell with 3 × 3 × 1 **k** sampling, and a force cutoff distance of 0.6 nm was employed. The ShengBTE package[38] was used for iteratively solving the phonon BTE.[42] Considering the melting point of bulk Te is about 723 K, the thermoelectric properties of monolayer $\alpha$-Te are discussed between 300 and 700 K. Here, we focus on the bulk transport properties of $\alpha$-Te, a 2D hexagonal lattice structure with infinite in-plane extension. The isotropy of in-plane bulk transport properties is guaranteed by the lattice symmetry. The impact of zigzag and armchair configurations, which may yield directional transport properties in nanoribbons, is thus not relevant in this work. Thus, the electrical and thermal transport properties of monolayer $\alpha$-Te in the basal plane are regarded as scalars hereafter.

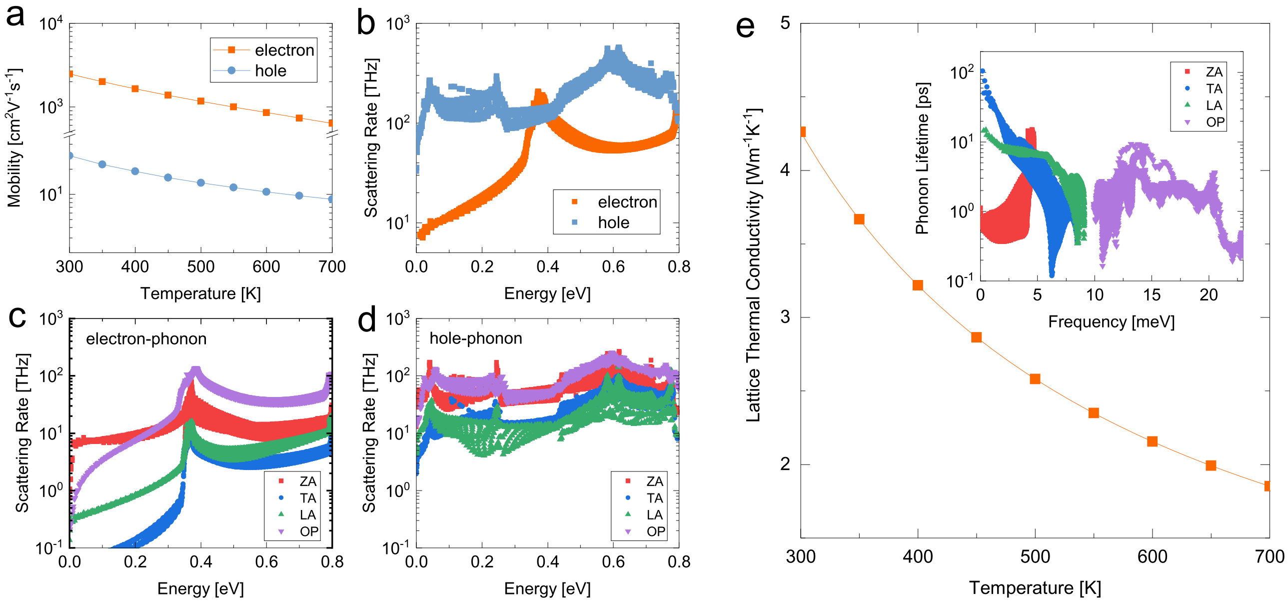

**Figure 2.** (a) Intrinsic electron and hole mobilities of $\alpha$-Te as a function of temperatures. (b) Electron and hole scattering rates at room temperature, and the (c, d) corresponding decoupled scattering contributed from different phonon modes for electrons and holes, respectively. (e) Lattice thermal conductivity and the room-temperature phonon lifetimes of different modes.

## 3. RESULTS AND DISCUSSION

**3.1. Mobility and Lattice Thermal Conductivity.** The calculated band structure of $\alpha$-Te with the spin-orbit coupling (SOC) considered is shown in Figure 1b. As shown, the SOC significantly alters the band structure. Since the electrical transport properties are markedly affected by the band structure,[35,43] the SOC must be included to achieve high accuracy for the calculated mobility. $\alpha$-Te has an indirect band gap, about 0.37 eV, with the conduction band minimum (CBM) located at Γ and the valence band maximum (VBM) located in the Γ−M line and its equivalent positions in the first Brillouin zone. Since LDA underestimates the band gap, the GW correction was employed using YAMBO code,[44] and the band gap is opened up to 0.69 eV (cf. Figure S1 in the Supporting Information), only a little smaller than the previous calculation (0.75 eV)[23] using VASP[45] with HSE06 functional[46] including SOC. The real band gap is 10 times larger than thermalization energy below 700 K, *i.e.*, $10k_BT \approx 0.60$ eV, thus the bipolar effect is negligible in the electrical transport.[47,48] Therefore, the electron and hole transports were calculated using conduction and valence bands separately, with chemical potential manually shifted with respect to CBM and VBM, respectively.

The band structure is flatter near the VBM compared to that near the CBM, suggesting a larger effective mass for VBM. In previous studies, the valence and conduction bands around band edges were treated as isotropic.[23,27] However, we found that such isotropy is oversimplified for holes. As seen in the energy-momentum contours of Figure 1c,d, the CBM edge is indeed isotropic with an effective mass of $0.10m_e$, in agreement with previous results.[23,27] However, the VBM edge is strongly anisotropic, with $m_x^* = 0.39m_e$ and $m_y^* = 0.17m_e$ when fitting the valley in the Γ−M line along the $x$ and $y$ directions. Previous studies only fitted the hole effective mass along the Γ−M line, *i.e.*, $m_y^*$, and reported similar values.[23,27] It is important to note that despite the anisotropic shape of each hole pocket, and thus anisotropic hole effective masses along the $x$ and $y$ axes, as shown in Figure 1d, the hole transport properties are isotropic in the basal plane due to the crystal lattice symmetry embodied in the space group $P\bar{3}m1$ (#164) of $\alpha$-Te. Figure 1e shows the phonon dispersion of $\alpha$-Te. The maximum phonon frequency corresponds to an energy of 23 meV, smaller than most of the 2D materials[8−15] due to the heavy atomic mass of Te, but is comparable to other low $\kappa_L$ systems.[16−18] The low phonon frequency renders a low Debye temperature for $\alpha$-Te.

To calculate the carrier mobility, the **q** grids were interpolated to 120 × 120 × 1 for phonons, whereas the **k** grids were interpolated to 360 × 360 × 1 and 120 × 120 × 1 for electrons and holes, respectively, which are enough to ensure the convergence (cf. Figure S2 in the Supporting Information). The calculated intrinsic electron and hole mobilities of $\alpha$-Te at different temperatures are plotted in Figure 2a. Remarkably, the room-temperature electron mobility reaches as high as 2500 cm$^2$ V$^{-1}$ s$^{-1}$, outperforming many other 2D materials such as TMDs,[34,49] InSe,[50] black phosphorene,[49,51] and antimony.[52] Meanwhile, this electron mobility is about two orders of magnitude larger than the hole mobility, which is only about 30 cm$^2$ V$^{-1}$ s$^{-1}$ at room temperature. This tallies with the usual situation that materials have high mobility for only one type of carrier, such as Si,[35,43] GaAs,[35] SiC,[53] GaN,[54] InSe,[50] and so on. We note that the estimations based on a simplified phenomenological model with isotropic parabolic bands and acoustic deformation potentials correctly give a high electron mobility (~2100 cm$^2$ V$^{-1}$ s$^{-1}$).[23,27] This is expected because the electron transport at low temperatures with a low carrier concentration is mainly governed by the low-energy electrons in the Γ valley, reasonably described by the isotropic parabolic relation. Nonetheless, the deformation potential model is crude, which completely ignores the nonparabolicity of the band structure, the mode- and temperature-dependences of electron−phonon scattering, to name a few. For instance, using the acoustic deformation potential model, the electron mobility of monolayer $MoS_2$ is either overestimated by twice[55] or underestimated by half[56] as compared to the first-principles

https://dx.doi.org/10.1021/acsami.0c10236
ACS Appl. Mater. Interfaces 2020, 12, 43901−43910

calculations.[34] It can be seen that the hole mobility of $\alpha$-Te is overestimated (~1700 $cm^2\ V^{-1}\ s^{-1}$)[23,27] by about two orders of magnitude.

The remarkably smaller hole mobility as compared to the electron is due to the heavier effective mass, which results in not only a smaller group velocity but also much stronger scattering rates. As shown in Figure 2b, the scattering rates of electrons at room temperature are much lower than those of holes, except in a narrow neighborhood of 0.4 eV. The scattering rates of electrons are also lower than that of $MoS_2$,[34] InSe,[50] and black phosphorene.[51] This is a combined consequence of a small effective mass and a low Debye temperature. The electron−phonon scattering process requires energy and momentum conservations between electrons and phonons. Generally, the closer the difference in the energy scale between the electron and the phonon, the more easily the conservation criteria can be satisfied. The characteristic energy scale of electrons (on the Fermi level) is on the order of eV, while the counterpart of phonons varies between 1 and 100 meV. A lower Debye temperature generally corresponds to lower phonon energies, thus a larger energy difference between electrons and phonons and a smaller scattering phase space. In this case, the scattering rates are expected to be small and favors the electrical conductivity. By looking into the decomposed contribution to the scattering rates from out-of-plane acoustic (ZA), transverse acoustic (TA), longitudinal acoustic (LA), and optical (OP) phonons in Figure 2c,d, we can see that the ZA and OP phonons contribute the most at relatively low energies, while the contribution of TA and LA increases as the energy increases. Unlike $MoS_2$ but as in silicene and stanene,[57−59] ZA contributes significantly to the scattering, which originates from the broken mirror symmetry of the crystal structure.[60] For 2D systems with mirror symmetry, the ZA phonons have purely out-of-plane polarization vectors and the in-plane Bloch waves are mirror symmetric; therefore, the electrons and ZA phonons are decoupled to the first order and the coupling matrix elements vanish. On the other hand, in buckled 2D systems, where the mirror symmetry is broken, the cancelation no longer applies.

The temperature-dependent $\kappa_L$ of $\alpha$-Te was calculated, as shown in Figure 2e, with a value of 4.2 $W\ m^{-1}\ K^{-1}$ at 300 K and 1.8 $W\ m^{-1}\ K^{-1}$ at 700 K, which are about half smaller than the values reported by Gao et al.[27] We have carefully checked the convergence of $\kappa_L$ (cf. Figures S3 and S4 in the Supporting Information), and found that the calculated $\kappa_L$ would be overestimated if the computational parameters especially the scalebroad used in ShengBTE package[38] are insufficient for the convergence. $\kappa_L$ of monolayer $\alpha$-Te is much smaller than monolayer TMDs,[29,30] black phoshperene,[61] InSe,[62] but close to the recently reported thermoelectric monolayer of $Bi_2Te_2X$ (X = S, Se, Te),[18] $\beta$-Te,[26] and organic $(NiC_4S_4)_n$.[63] The low $\kappa_L$ is due to a low Debye temperature, which suggests a small group velocity and small phonon lifetimes.[64,65] $\kappa_L$ is mainly contributed by phonons with a relaxation time below 100 ps at room temperature, as shown in the inset of Figure 2e, which is smaller than the monolayer TMDs,[30] InSe,[62] and $\beta$-Te.[26] The acoustic phonons, of which the frequency is smaller than 10 meV, contribute more than 70% of $\kappa_L$ above room temperature.

### 3.2. Thermoelectric Figure of Merit.

The high electron mobility and low lattice thermal conductivity are key ingredients for high $ZT$. The carrier concentration dependence of $ZT$ was calculated at a number of temperatures and is shown in Figure 3. It can be seen that $\alpha$-Te indeed exhibits high $ZT$, up to 1.46 at 700 K under an electron concentration of $1 \times 10^{19}$ $cm^{-3}$ in the case of n-type $\alpha$-Te. As temperature decreases, the maximum $ZT$ is reduced. However, at 300 K, it is still as large as 0.55 at an electron concentration of $5 \times 18^{18}$ $cm^{-3}$. The $ZT$ of p-type $\alpha$-Te was also calculated, which is much smaller than the n-type counterpart at the same carrier concentration because of the much lower hole mobility. Nonetheless, as the hole concentration increases to $5 \times 10^{20}$ $cm^{-3}$, the maximum $ZT$ of p-type $\alpha$-Te can reach 0.86 at 700 K, whereas the highest room-temperature value is about 0.25 at a hole concentration of $2.5 \times 10^{20}$ $cm^{-3}$. It is also found that the optimal carrier concentrations of unstrained $\alpha$-Te are (5−10) $\times 10^{18}$ $cm^{-3}$ for the n-type and (2.5−5) $\times 10^{20}$ $cm^{-3}$ for the p-type $\alpha$-Te over the whole temperature range of 300−700 K.

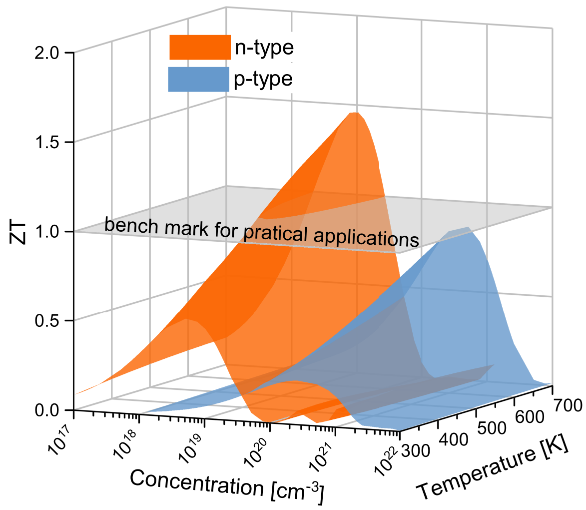

**Figure 3.** Thermoelectric $ZT$ of n- and p-type $\alpha$-Te as a function of carrier concentrations and temperatures.

Figure 4 provides the individual thermoelectric properties of n- and p-type $\alpha$-Te as a function of carrier concentrations at 300 and 700 K. For an n-type system, in Figure 4a,b, as electron concentration increases, $S$ decreases while $\sigma$ and $\kappa_e$ increase; consequently, the PF and $ZT$ have a peak shape as the function of carrier concentrations. At 300 K, $S$ and $\sigma$ at the optimal concentration of $ZT$ are 218 $\mu V\ K^{-1}$ and 1943 $S\ cm^{-1}$, respectively, producing remarkably high PF of 92 $\mu W\ cm^{-1}\ K^{-2}$. As temperature increases, $S$ is slightly increased while $\sigma$ is significantly reduced, and thus the PF is decreased. At 700 K, the PF at the optimal carrier concentration of $ZT$ is approximately reduced by half to 50 $\mu W\ cm^{-1}\ K^{-2}$. The decrease of PF arises from a slight increase of $S$ to 227 $\mu V\ K^{-1}$ and a strong decline of $\sigma$ to 973 $S\ cm^{-1}$. The corresponding $\kappa_e$ is also reduced from 0.8 $W\ m^{-1}\ K^{-1}$ at 300 K to 0.6 $W\ m^{-1}\ K^{-1}$ 700 K; combined with the reduced $\kappa_L$, the total thermal conductivity is reduced by half. As shown in Figure 4c,d, the thermoelectric properties of p-type $\alpha$-Te exhibits similar concentration dependence and temperature dependence as their n-type counterparts. Specifically, at the optical carrier concentration of $ZT$, the PF of p-type $\alpha$-Te are 39 and 30 $\mu W\ cm^{-1}\ K^{-2}$ at 300 and 700 K, respectively, which are about half smaller than that of n-type $\alpha$-Te. Smaller PF of a p-type system leads to lower $ZT$. It is noted that at the optimal carrier concentration, the total thermal conductivity is mainly

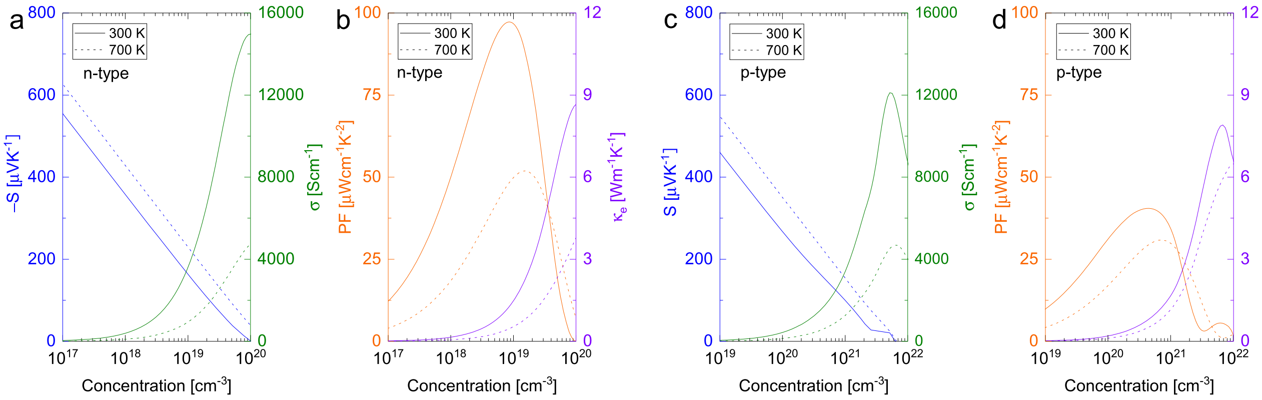

**Figure 4.** Seebeck coefficient ($S$), electrical conductivity ($\sigma$), electronic thermal conductivity ($\kappa_e$), and the power factor (PF) of (a, b) n- and (c, d) p-type $\alpha$-Te as a function of carrier concentrations at 300 and 700 K, respectively.

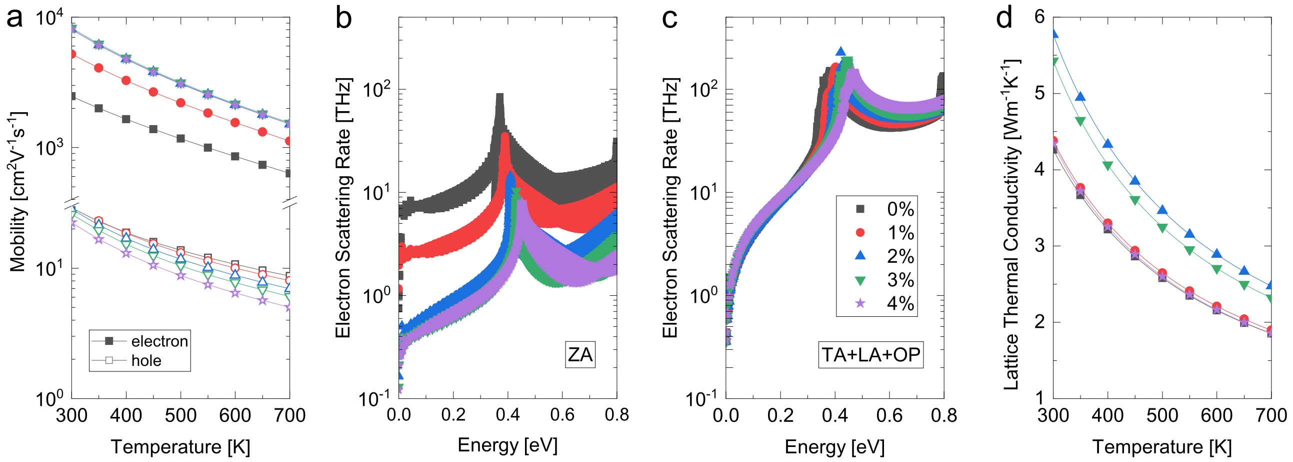

**Figure 5.** Tensile strain effect on (a) electron and hole mobilities, (b) electron scattering contributed by ZA phonons, (c) electron scattering contributed by TA, LA, and OP phonons, and (d) lattice thermal conductivity, respectively.

contributed by phonons. For instance, about 85 and 75% thermal conductivity is contributed by $\kappa_L$ at 300 and 700 K, respectively, for both n- and p-type systems.

### 3.3. Strain Effects.

Strain, which cannot be avoided in realistic samples, has important influence on the transport properties. It has been reported that the thermoelectric performance of monolayer $ZrS_2$, $TiS_2$, and InSe can be enhanced by tensile strain.[12,13,66] Therefore, we also studied the tensile strain effect on the properties of $\alpha$-Te for 1, 2, 3, and 4% strains. Figure 5a shows the tensile strain effect on electron and hole mobilities. It can be seen that the electron mobilities increase significantly, which reach up to 8000 cm$^2$ V$^{-1}$ s$^{-1}$ at room temperature above 2% strain. As temperature increases to 700 K, the enhancement of electron mobility by tensile strain is reduced, but still more than doubled as compared to an unstrained system, from 630 to 1515 cm$^2$ V$^{-1}$ s$^{-1}$. It is also found that the electron mobilities under 2, 3, and 4% strains are almost identical, indicating that strain effect gets marginal above 2% strain.

The tensile strain effect on mobility can be understood from the variations of the band structures (Figures S5−S7 in the Supporting Information) and the scattering rates, as shown in Figure 5b,c. It is found that the electron effective mass is only slightly reduced. For an unstrained system, the ZA phonons dominate the scattering of electrons at low energies as compared to other phonon modes, partially because of the divergent thermal population of the quadratic ZA phonons.[60] Upon strain, the ZA phonons get stiffened, and the dispersion changes from quadratic to linear (Figure S8 in the Supporting Information). Consequently, the thermal population of the quadratic ZA phonons is significantly reduced. Therefore, the scattering rates by ZA phonons decrease by more than one order of magnitude at 2, 3, and 4% strains. For a given electron state, smaller effective mass means fewer electron states available for phonon scattering in the momentum space. The small scattering phase space corresponds to a small scattering rate. The scattering rates by TA, LA, and OP phonons are almost unchanged, implying the weak effect from the change of electron effective mass. Therefore, the significant enhancement of electron mobility stems from the great decrease of electron−ZA phonons scattering. As for holes, we found that the tensile strain also reduces the scattering rates by ZA phonons, but increases the scattering rates by other phonons (Figure S9 in the Supporting Information) due to the equivalently increased hole effective mass. Since the ZA phonons scattering is not dominant for holes, the total scattering rates of holes are increased. As a result, the hole mobilities under tensile strains decrease slightly, for instance, from 30 to 23 cm$^2$ V$^{-1}$ s$^{-1}$ by 4% strain at room temperature. Unlike electron mobilities, the change of $\kappa_L$ caused by tensile strain is also not strong. At room temperature, $\kappa_L$ first increases from 4.2 to 5.7 W m$^{-1}$ K$^{-1}$ with 2% strain and decreases again to 4.3 W m$^{-1}$ K$^{-1}$ at 4% strain, which is a result of the complicated change of mode-dependent phonon group velocity and phonon lifetime.

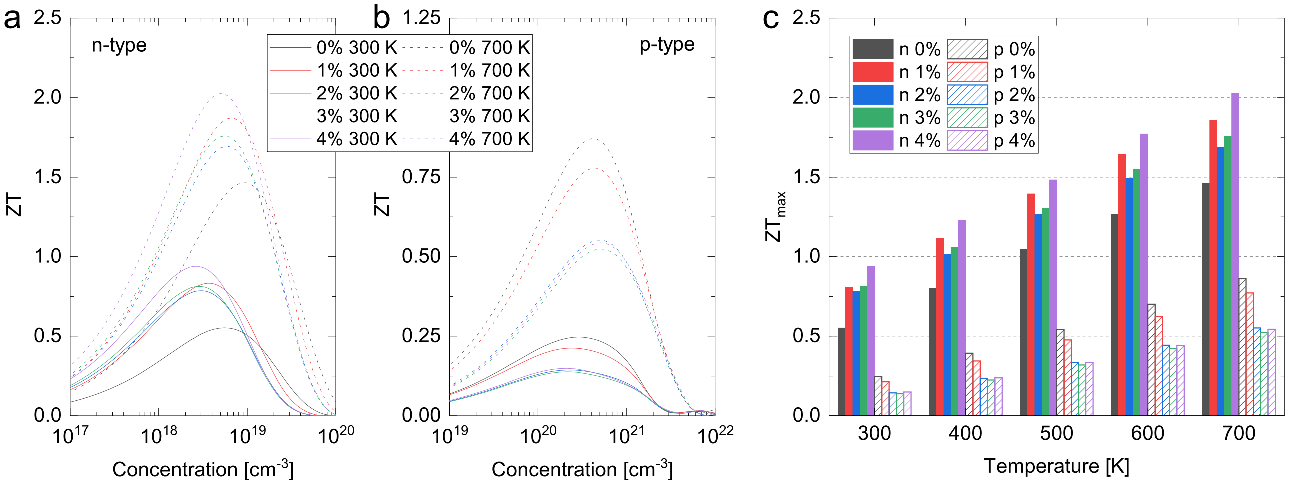

**Figure 6.** Concentration dependence of the *ZT* for (a) n- and (b) p-type $\alpha$-Te under different tensile strains at 300 and 700 K, respectively. (c) Maximum *ZT* under different tensile strains for n- and p-type $\alpha$-Te at different temperatures.

The effect of compressive strain is also studied. It is found that −1% compressive strain has limited effects on the electronic band structure near the band edges (Figure S5 in the Supporting Information), but results in imaginary frequencies of ZA phonons near the Γ point (Figure S8 in the Supporting Information). Imaginary frequencies are not allowed in the calculations of electron−phonon coupling; with the imaginary ZA modes manually removed, the resulting electron mobility is significantly enhanced, while the hole mobility is much less affected (Figure S10 in the Supporting Information). Although the physical meaning is discounted because imaginary phonon modes do not exist in real life materials, these results attest to the vital role of the coupling between electrons and the ZA modes in relation to the electron mobility (Figure S11 in the Supporting Information). In short, any strain-induced change to the ZA phonon modes would drastically impact the electron mobility. It should be noted that the strain effect on carrier mobility has a different origin in monolayer $\alpha$-Te and bulk GaN. Poncé et al.[54] reported that the hole mobility of bulk GaN can be significantly increased by both tensile and compressive strains due to the upshift of the light split-off hole band. These results showcased the efficacy of strain in tuning the electronic band structure of materials with multiple bands close in energy but differing in the effective mass. By contrast, the electronic bands of $\alpha$-Te are well separated in energy and the strain effect is limited. Rather, the strain effect of electron mobility in $\alpha$-Te is governed by the strain effect of the ZA phonon modes and the resulting change of electron−phonon scattering.

The noticeably increased electron mobility portends significant increase of $\sigma$ and $\kappa_e$ in a n-type system, whereas *S* is only weakly affected since it is mainly determined by the band structure;[67] as a consequence, loosely speaking, the overall trend of PF is increased (Figure S12 in the Supporting Information). As discussed above, $\kappa$ is dominated by $\kappa_L$ that is less changed upon strain. The *ZT* of n-type $\alpha$-Te is generally enhanced by the tensile strain, as shown in Figure 6a. The optimal concentration of n-type $\alpha$-Te varies only slightly with 1−4% tensile strain in the range of $(2.5{-}7.5) \times 10^{18}$ cm$^{-3}$ over the temperature range of 300−700 K. By contrast, $\sigma$ and PF of p-type $\alpha$-Te are decreased by tensile strain (Figure S13 in the Supporting Information), in consistence with the reduced hole mobility, and the *ZT* becomes worse, as shown in Figure 6b. The optimal concentration of p-type $\alpha$-Te is also weakly affected by the tensile strain in the range of $(2.5{-}5) \times 10^{20}$ cm$^{-3}$ over the temperature range of 300−700 K. Figure 6c shows the maximum *ZT* under different strains and temperatures for n- and p-type $\alpha$-Te. The maximum *ZT* of the n-type system increases first at 1% strain due to the increase of $\sigma$, but decreases at 2 and 3% strains due to the increase of $\kappa_L$. When the strain increases up to 4%, the *ZT* increases again because $\kappa_L$ reduces to the level of no strain. At room temperature, the enhanced *ZT* is 0.94. When temperature increases to 700 K, the optimal *ZT* can be as high as 2.03, which is comparable with the famous bulk thermoelectric SnSe at close temperatures.[68,69] In contrast, it is found that the *ZT* of a p-type system is decreased by tensile strain due to its deteriorated hole transport properties. From the concentration and temperature dependences of the calculated *ZT* of 4% strained n-type $\alpha$-Te, it is found that the *ZT* can be larger than unity over a wide electron concentration and temperature ranges, promising realistic applications. The thermoelectric *ZT* of n-type $\alpha$-Te is much better than previously estimated $\beta$-Te[28] due to its much smaller effective mass and the promising strain effect.

## 4. CONCLUSIONS

In summary, the intrinsic electrical and thermal transport properties of monolayer $\alpha$-Te were studied based on parameter-free first-principles calculations and solving the electron−phonon-limited Boltzmann transport equation. It is found that $\alpha$-Te has ultrahigh electron mobility despite hole mobility that is two orders of magnitude lower. The room-temperature electron and hole mobilities are 2500 and 30 cm$^2$ V$^{-1}$ s$^{-1}$, respectively. Because of the absence of mirror symmetry in the crystal structure, the heavily populated out-of-plane acoustic (ZA) phonons play a key role in the scattering of a charge carrier. Meanwhile, the lattice thermal conductivity of $\alpha$-Te is lower than many previously reported monolayer materials due to its low phonon frequency and short phonon lifetime. Above room temperature, the lattice thermal conductivity is lower than 4.2 W m$^{-1}$ K$^{-1}$. As a result, monolayer $\alpha$-Te displays good thermoelectric performance; the *ZT* value reaches 1.46 and 0.86 at 700 K for pristine n- and p-type systems, respectively, while the room-temperature counterparts are 0.55 and 0.25. Notably, the tensile strain

https://dx.doi.org/10.1021/acsami.0c10236

significantly enhances the *ZT* of an n-type system mainly due to strain-induced linear dispersion of ZA modes and the resulting suppressed carrier scattering by ZA modes. The peak *ZT* values are enhanced to 0.94 and 2.03 by a 4% tensile strain at 300 and 700 K, respectively. By contrast, strain degrades the thermoelectric performance of p-type monolayer $\alpha$-Te. These results are expected to promote the experimental study of monolayer $\alpha$-Te via doping, alloying, and compositing.

## ■ ASSOCIATED CONTENT

### Supporting Information

The Supporting Information is available free of charge at https://pubs.acs.org/doi/10.1021/acsami.0c10236.

> The band structure with GW correction, convergence check for mobility, convergence check for lattice thermal conductivity, the strain effect on the band structure, the strain effect on phonon dispersion, scattering rates of holes under tensile strain, mobility under compressive strain, the tensile strain effect on thermoelectric properties, and thermoelectric *ZT* with closed-circuit electronic thermal conductivity (PDF)

## ■ AUTHOR INFORMATION

### Corresponding Author

**Wu Li** − *Institute for Advanced Study, Shenzhen University, Shenzhen 518060, China*; Email: wu.li.phys2011@gmail.com

### Authors

**Jinlong Ma** − *Institute for Advanced Study, Shenzhen University, Shenzhen 518060, China; School of Energy and Power Engineering, Huazhong University of Science and Technology, Wuhan 430074, China;* orcid.org/0000-0003-3009-2084

**Fanchen Meng** − *Department of Physics and Astronomy, Clemson University, Clemson, South Carolina 29634, United States*

**Jian He** − *Department of Physics and Astronomy, Clemson University, Clemson, South Carolina 29634, United States;* orcid.org/0000-0002-6377-3022

**Yu Jia** − *International Laboratory for Quantum Functional Materials of Henan, and School of Physics and Engineering, Zhengzhou University, Zhengzhou 450001, China*

Complete contact information is available at: https://pubs.acs.org/10.1021/acsami.0c10236

### Notes

The authors declare no competing financial interest.

## ■ ACKNOWLEDGMENTS

J.M. acknowledges support from the National Natural Science Foundation of China (No. 11804229). W.L. acknowledges support from the Shenzhen Science, Technology and Innovation Commission (No. JCYJ20170412105922384), the National Natural Science Foundation of China (No. 11704258), and the Natural Science Foundation of Guangdong Province (No. 2017A030310377).

## ■ REFERENCES

(1) He, J.; Tritt, T. M. Advances in Thermoelectric Materials Research: Looking Back and Moving Forward. *Science* **2017**, *357*, No. eaak9997.

(2) Snyder, G. J.; Toberer, E. S. Complex Thermoelectric Materials. *Nat. Mater.* **2008**, *7*, 105−114.

(3) Zhu, T.; Liu, Y.; Fu, C.; Heremans, J. P.; Snyder, J. G.; Zhao, X. Compromise and Synergy in High-Efficiency Thermoelectric Materials. *Adv. Mater.* **2017**, *29*, No. 1605884.

(4) Dehkordi, A. M.; Zebarjadi, M.; He, J.; Tritt, T. M. Thermoelectric Power Factor: Enhancement Mechanisms and Strategies for Higher Performance Thermoelectric Materials. *Mater. Sci. Eng., R* **2015**, *97*, 1−22.

(5) Zeng, J.; He, X.; Liang, S.-J.; Liu, E.; Sun, Y.; Pan, C.; Wang, Y.; Cao, T.; Liu, X.; Wang, C.; et al. Experimental Identification of Critical Condition for Drastically Enhancing Thermoelectric Power Factor of Two-Dimensional Layered Materials. *Nano Lett.* **2018**, *18*, 7538−7545.

(6) Yoshida, M.; Iizuka, T.; Saito, Y.; Onga, M.; Suzuki, R.; Zhang, Y.; Iwasa, Y.; Shimizu, S. Gate-Optimized Thermoelectric Power Factor in Ultrathin $WSe_2$ Single Crystals. *Nano Lett.* **2016**, *16*, 2061−2065.

(7) Hippalgaonkar, K.; Wang, Y.; Ye, Y.; Qiu, D. Y.; Zhu, H.; Wang, Y.; Moore, J.; Louie, S. G.; Zhang, X. High Thermoelectric Power Factor in Two-Dimensional Crystals of $MoS_2$. *Phys. Rev. B* **2017**, *95*, No. 115407.

(8) Huang, W.; Da, H.; Liang, G. Thermoelectric Performance of $MX_2$ (M = Mo,W; X = S,Se) Monolayers. *J. Appl. Phys.* **2013**, *113*, No. 104304.

(9) Gandi, A. N.; Schwingenschlögl, U. $WS_2$ as An Excellent High-Temperature Thermoelectric Material. *Chem. Mater.* **2014**, *26*, 6628−6637.

(10) Kumar, S.; Schwingenschlögl, U. Thermoelectric Response of Bulk and Monolayer $MoSe_2$ and $WSe_2$. *Chem. Mater.* **2015**, *27*, 1278−1284.

(11) Gandi, A. N.; Alshareef, H. N.; Schwingenschlögl, U. Thermoelectric Performance of the MXenes $M_2CO_2$ (M = Ti, Zr, or Hf). *Chem. Mater.* **2016**, *28*, 1647−1652.

(12) Li, G.; Yao, K.; Gao, G. Strain-Induced Enhancement of Thermoelectric Performance of $TiS_2$ Monolayer Based on First-Principles Phonon and Electron Band Structures. *Nanotechnology* **2018**, *29*, No. 015204.

(13) Lv, H. Y.; Lu, W. J.; Shao, D. F.; Lu, H. Y.; Sun, Y. P. Strain-Induced Enhancement in the Thermoelectric Performance of A $ZrS_2$ Monolayer. *J. Mater. Chem. C* **2016**, *4*, 4538−4545.

(14) Zhang, J.; Liu, X.; Wen, Y.; Shi, L.; Chen, R.; Liu, H.; Shan, B. Titanium Trisulfide Monolayer as A Potential Thermoelectric Material: A First-Principles-Based Boltzmann Transport Study. *ACS Appl. Mater. Interfaces* **2017**, *9*, 2509−2515.

(15) Peng, B.; Zhang, H.; Shao, H.; Xu, K.; Ni, G.; Li, J.; Zhu, H.; Soukoulis, C. M. Chemical Intuition for High Thermoelectric Performance in Monolayer Black Phosphorus, a-Arsenene and aW-Antimonene. *J. Mater. Chem. A* **2018**, *6*, 2018−2033.

(16) Marfoua, B.; Hong, J. High Thermoelectric Performance in Hexagonal 2D $PdTe_2$ Monolayer at Room Temperature. *ACS Appl. Mater. Interfaces* **2019**, *11*, 38819−38827.

(17) Moujaes, E. A.; Diery, W. A. Thermoelectric Properties of 1T Monolayer Pristine and Janus Pd Dichalcogenides. *J. Phys.: Condens. Matter* **2019**, *31*, No. 455502.

(18) Rashid, Z.; Nissimagoudar, A. S.; Li, W. Phonon Transport and Thermoelectric Properties of Semiconducting $Bi_2Te_2X$ (X = S, Se, Te) Monolayers. *Phys. Chem. Chem. Phys.* **2019**, *21*, 5679−5688.

(19) Peng, B.; Mei, H.; Zhang, H.; Shao, H.; Xu, K.; Ni, G.; Jin, Q.; Soukoulis, C. M.; Zhu, H. High Thermoelectric Efficiency in Monolayer $PbI_2$ from 300 K to 900 K. *Inorg. Chem. Front.* **2019**, *6*, 920−928.

(20) Zhang, X.; Liu, C.; Tao, Y.; Li, Y.; Guo, Y.; Chen, Y.; Zeng, X. C.; Wang, J. High ZT 2D Thermoelectrics by Design: Strong Interlayer Vibration and Complete Band-Extrema Alignment. *Adv. Funct. Mater.* **2020**, *30*, No. 2001200.

(21) Gao, Z.; Wang, J.-S. Thermoelectric Penta-Silicene with a High Room-Temperature Figure of Merit. *ACS Appl. Mater. Interfaces* **2020**, *12*, 14298−14307.

(22) Lin, S.; Li, W.; Chen, Z.; Shen, J.; Ge, B.; Pei, Y. Tellurium as A High-Performance Elemental Thermoelectric. *Nat. Commun.* **2016**, *7*, No. 10287.

(23) Zhu, Z.; Cai, X.; Yi, S.; Chen, J.; Dai, Y.; Niu, C.; Guo, Z.; Xie, M.; Liu, F.; Cho, J.-H.; Jia, Y.; Zhang, Z. Multivalency-Driven Formation of Te-Based Monolayer Materials: A Combined First-Principles and Experimental Study. *Phys. Rev. Lett.* **2017**, *119*, No. 106101.

(24) Chen, J.; Dai, Y.; Ma, Y.; Dai, X.; Ho, W.; Xie, M. Ultrathin $\beta$-tellurium Layers Grown on Highly Oriented Pyrolytic Graphite by Molecular-Beam Epitaxy. *Nanoscale* **2017**, *9*, 15945−15948.

(25) Huang, X.; Guan, J.; Lin, Z.; Liu, B.; Xing, S.; Wang, W.; Guo, J. Epitaxial Growth and Band Structure of te Film on Graphene. *Nano Lett.* **2017**, *17*, 4619−4623.

(26) Gao, Z.; Tao, F.; Ren, J. Unusually Low Thermal Conductivity of Atomically Thin 2D Tellurium. *Nanoscale* **2018**, *10*, 12997−13003.

(27) Gao, Z.; Liu, G.; Ren, J. High Thermoelectric Performance in Two-Dimensional Tellurium: An Ab Initio Study. *ACS Appl. Mater. Interfaces* **2018**, *10*, 40702−40709.

(28) Sharma, S.; Singh, N.; Schwingenschlögl, U. Two-Dimensional Tellurene as Excellent Thermoelectric Material. *ACS Appl. Energy Mater.* **2018**, *1*, 1950−1954.

(29) Li, W.; Carrete, J.; Mingo, N. Thermal Conductivity and Phonon Linewidths of Monolayer $MoS_2$ from First Principles. *Appl. Phys. Lett.* **2013**, *103*, No. 253103.

(30) Gu, X.; Yang, R. Phonon Transport in Single-Layer Transition Metal Dichalcogenides: A First-Principles Study. *Appl. Phys. Lett.* **2014**, *105*, No. 131903.

(31) Giustino, F. Electron−phonon Interactions from First Principles. *Rev. Mod. Phys.* **2017**, *89*, No. 015003.

(32) Poncé, S.; Li, W.; Reichardt, S.; Giustino, F. First-principles Calculations of Charge Carrier Mobility and Conductivity in Bulk Semiconductors and Two-Dimensional Materials. *Rep. Prog. Phys.* **2020**, *83*, No. 036501.

(33) Qiu, B.; Tian, Z.; Vallabhaneni, A.; Liao, B.; Mendoza, J. M.; Restrepo, O. D.; Ruan, X.; Chen, G. First-Principles Simulation of Electron Mean-Free-Path Spectra and Thermoelectric Properties in Silicon. *Europhys. Lett.* **2015**, *109*, No. 57006.

(34) Li, W. Electrical Transport Limited by Electron−Phonon Coupling from Boltzmann Transport Equation: An Ab Initio Study of Si, Al, and $MoS_2$. *Phys. Rev. B* **2015**, *92*, No. 075405.

(35) Ma, J.; Nissimagoudar, A. S.; Li, W. First-Principles Study of Electron and Hole Mobilities of Si and GaAs. *Phys. Rev. B* **2018**, *97*, No. 045201.

(36) Poncé, S.; Margine, E.; Verdi, C.; Giustino, F. EPW: Electron−Phonon Coupling, Transport and Superconducting Properties Using Maximally Localized Wannier Functions. *Comput. Phys. Commun.* **2016**, *209*, 116−133.

(37) Madsen, G. K. H.; Singh, D. J. BoltzTraP. A Code for Calculating Band-Structure Dependent Quantities. *Comput. Phys. Commun.* **2006**, *175*, 67−71.

(38) Li, W.; Carrete, J.; Katcho, N. A.; Mingo, N. ShengBTE: A Solver of The Boltzmann Transport Equation for Phonons. *Comput. Phys. Commun.* **2014**, *185*, 1747−1758.

(39) Cahill, D. G.; Braun, P. V.; Chen, G.; Clarke, D. R.; Fan, S.; Goodson, K. E.; Keblinski, P.; King, W. P.; Mahan, G. D.; Majumdar, A.; Maris, H. J.; Phillpot, S. R.; Pop, E.; Shi, L. Nanoscale thermal transport. II. 2003-2012. *Appl. Phys. Rev.* **2014**, *1*, No. 011305.

(40) Giannozzi, P.; Andreussi, O.; Brumme, T.; Bunau, O.; Nardelli, M. B.; Calandra, M.; Car, R.; Cavazzoni, C.; Ceresoli, D.; Cococcioni, M.; et al. Advanced Capabilities for Materials Modelling with Quantum ESPRESSO. *J. Phys.: Condens. Matter* **2017**, *29*, No. 465901.

(41) Perdew, J. P.; Zunger, A. Self-Interaction Correction to Density-Functional Approximations for Many-Electron Systems. *Phys. Rev. B* **1981**, *23*, 5048−5079.

(42) Ma, J.; Li, W.; Luo, X. Examining the Callaway Model for Lattice Thermal Conductivity. *Phys. Rev. B* **2014**, *90*, No. 035203.

(43) Poncé, S.; Margine, E. R.; Giustino, F. Towards Predictive Many-Body Calculations of Phonon-Limited Carrier Mobilities in Semiconductors. *Phys. Rev. B* **2018**, *97*, No. 121201(R).

(44) Marini, A.; Hogan, C.; Gruning, M.; Varsano, D. Yambo: An Ab Initio Tool for Excited State Calculations. *Comput. Phys. Commun.* **2009**, *180*, 1392−1403.

(45) Blöchl, P. E. Projector Augmented-Wave Method. *Phys. Rev. B* **1994**, *50*, 17953−17979.

(46) Heyd, J.; Scuseria, G. E.; Ernzerhof, M. Hybrid Functionals Based on A Screened Coulomb Potential. *J. Chem. Phys.* **2003**, *118*, 8207−8215.

(47) Tritt, T. M.; Subramanian, M. A. Thermoelectric Materials, Phenomena, and Applications: A Bird's Eye View. *MRS Bull.* **2006**, *31*, 188−198.

(48) Ma, J.; Nissimagoudar, A. S.; Wang, S.; Li, W. High Thermoelectric Figure of Merit of Full-Heusler $Ba_2AuX$ (X = As, Sb, and Bi). *Phys. Status Solidi RRL* **2020**, *14*, No. 2000084.

(49) Sohier, T.; Campi, D.; Marzari, N.; Gibertini, M. Mobility of Two-Dimensional Materials from First Principles in An Accurate and Automated Framework. *Phys. Rev. Mater.* **2018**, *2*, No. 114010.

(50) Li, W.; Ponc, S.; Giustino, F. Dimensional Crossover in the Carrier Mobility of Two-Dimensional Semiconductors: The Case of InSe. *Nano Lett.* **2019**, *19*, 1774−1781.

(51) Liao, B.; Zhou, J.; Qiu, B.; Dresselhaus, M. S.; Chen, G. Ab Initio Study of Electron−Phonon Interaction in Phosphorene. *Phys. Rev. B* **2015**, *91*, No. 235419.

(52) Cheng, L.; Zhang, C.; Liu, Y. The Optimal Electronic Structure for High-Mobility 2D Semiconductors: Exceptionally High Hole Mobility in 2D Antimony. *J. Am. Chem. Soc.* **2019**, *141*, 16296−16302.

(53) Meng, F.; Ma, J.; He, J.; Li, W. Phonon-Limited Carrier Mobility and Temperature-Dependent Scattering Mechanism of 3C-SiC from First Principles. *Phys. Rev. B* **2019**, *99*, No. 045201.

(54) Poncé, S.; Jena, D.; Giustino, F. Hole Mobility of Strained GaN from First Principles. *Phys. Rev. B* **2019**, *100*, No. 085204.

(55) Zhang, W.; Huang, Z.; Zhang, W.; Li, Y. Two-dimensional Semiconductors with Possible High Room Temperature Mobility. *Nano Res.* **2014**, *7*, 1731−1737.

(56) Cai, Y.; Zhang, G.; Zhang, Y.-W. Polarity-Reversed Robust Carrier Mobility in Monolayer $MoS_2$ Nanoribbons. *J. Am. Chem. Soc.* **2014**, *136*, 6269−6275.

(57) Gunst, T.; Markussen, T.; Stokbro, K.; Brandbyge, M. First-Principles Method for Electron−Phonon Coupling and Electron Mobility: Applications to Two-Dimensional Materials. *Phys. Rev. B* **2016**, *93*, No. 035414.

(58) Li, X.; Mullen, J. T.; Jin, Z.; Borysenko, K. M.; Buongiorno Nardelli, M.; Kim, K. W. Intrinsic Electrical Transport Properties of Monolayer Silicene and $MoS_2$ from First Principles. *Phys. Rev. B* **2013**, *87*, No. 115418.

(59) Nakamura, Y.; Zhao, T.; Xi, J.; Shi, W.; Wang, D.; Shuai, Z. Intrinsic Charge Transport in Stanene: Roles of Bucklings and Electron−Phonon Couplings. *Adv. Electron. Mater.* **2017**, *3*, No. 1700143.

(60) Fischetti, M. V.; Vandenberghe, W. G. Mermin-Wagner Theorem, Flexural Modes, and Degraded Carrier Mobility in Two-Dimensional Crystals with Broken Horizontal Mirror Symmetry. *Phys. Rev. B* **2016**, *93*, No. 155413.

(61) Qin, G.; Yan, Q.-B.; Qin, Z.; Yue, S.-Y.; Hu, M.; Su, G. Anisotropic Intrinsic Lattice Thermal Conductivity of Phosphorene from First Principles. *Phys. Chem. Chem. Phys.* **2015**, *17*, 4854−4858.

(62) Nissimagoudar, A. S.; Ma, J.; Chen, Y.; Li, W. Thermal Transport in Monolayer InSe. *J. Phys.: Condens. Matter* **2017**, *29*, No. 335702.

(63) Deng, T.; Yong, X.; Shi, W.; Gan, C. K.; Li, W.; Hippalgaonkar, K.; Zheng, J.-C.; Wang, X.; Yang, S.-W.; Wang, J.-S.; Wu, G. 2D Single-Layer $\pi$-Conjugated Nickel Bis(dithiolene) Complex: A Good-Electron-Poor-Phonon Thermoelectric Material. *Adv. Electron. Mater.* **2019**, *5*, No. 1800892.

(64) Li, W.; Mingo, N. Thermal Conductivity of Fully Filled Skutterudites: Role of the Filler. *Phys. Rev. B* **2014**, *89*, No. 184304.

(65) Li, W.; Mingo, N. Lattice Dynamics and Thermal Conductivity of Skutterudites $CoSb_3$ and $IrSb_3$ from First Principles: Why $IrSb_3$ Is A Better Thermal Conductor Than $CoSb_3$. *Phys. Rev. B* **2014**, *90*, No. 094302.

(66) Wang, Q.; Han, L.; Wu, L.; Zhang, T.; Li, S.; Lu, P. Strain Effect on Thermoelectric Performance of InSe Monolayer. *Nanoscale Res. Lett.* **2019**, *14*, No. 287.

(67) Ma, J.; Chen, Y.; Li, W. Intrinsic Phonon-Limited Charge Carrier Mobilities in Thermoelectric SnSe. *Phys. Rev. B* **2018**, *97*, No. 205207.

(68) Zhao, L.-D.; Tan, G.; Hao, S.; He, J.; Pei, Y.; Chi, H.; Wang, H.; Gong, S.; Xu, H.; Dravid, V. P.; Uher, C.; Snyder, G. J.; Wolverton, C.; Kanatzidis, M. G. Ultrahigh Power Factor and Thermoelectric Performance in Hole-Doped Single-Crystal SnSe. *Science* **2016**, *351*, 141−144.

(69) Chang, C.; Wu, M.; He, D.; Pei, Y.; Wu, C.-F.; Wu, X.; Yu, H.; Zhu, F.; Wang, K.; Chen, Y.; Huang, L.; Li, J.-F.; He, J.; Zhao, L.-D. 3D Charge and 2D Phonon Transports Leading to High Out-of-Plane ZT in N-type SnSe Crystals. *Science* **2018**, *360*, 778−783.